Detection and manipulation of the antiferromagnetic Néel vector in Cr_2O_3

Yi-Hui Zhang,[1,*] Tsao-Chi Chuang,[1,*] Danru Qu,[2,3,†] and Ssu-Yen Huang[1,3,‡]
[1]*Department of Physics, National Taiwan University, Taipei 106, Taiwan*
[2]*Center for Condensed Matter Sciences, National Taiwan University, Taipei 106, Taiwan*
[3]*Center of Atomic Initiative for New Materials, National Taiwan University, Taipei 106, Taiwan*

(Received 8 November 2021; revised 6 February 2022; accepted 14 March 2022; published 30 March 2022)

Detection and manipulation of the Néel vector in antiferromagnetic materials are promising for more stable, faster, and much higher-density spintronic devices. However, the electrical manipulation of the antiferromagnetic Néel vector remains challenging and controversial due to the difficulty in the detection of the zero net magnetization and the unavoidable complications from thermal artifacts. In this work, by utilizing the uniaxial antiferromagnet (AFM) Cr_2O_3, we demonstrate the detection and manipulation of the antiferromagnetic Néel vector. We reveal unambiguously the spin-dependent electrical responses of the coherent Cr_2O_3 Néel vector switching, where a symmetric Hall signal and a fourfold angular-dependent magnetoresistance are captured. We also demonstrate the in-plane arbitrary manipulation of the Cr_2O_3 Néel vector when the magnetocrystalline anisotropy energy is compensated. Our work for detecting and manipulating Néel vectors offers a critical guide for antiferromagnetic-based Néel vector switching exploration.

DOI: 10.1103/PhysRevB.105.094442

I. INTRODUCTION

Back in the 1970s, Louis Néel described antiferromagnets (AFMs) as "interesting but useless" materials in his Nobel prize lecture [1]. Due to the negligible magnetization and weak response to the external magnetic field, Néel vectors $\boldsymbol{n}_{\text{Néel}}$ in AFMs are hard to detect and manipulate. But in the last decade, intensive attention has been refocused on AFMs. The robustness against perturbations from the external magnetic field, the negligible stray field, and the ultrafast dynamics allow AFMs as key ingredients for more steadier, higher density, and much faster spintronic devices [2–4]. In 2014, Marti *et al.* indirectly manipulated the Néel vectors in FeRh by exploiting the first-order magnetic phase transition, allowing the write and read of the AFMs [5]. Soon after, several groups reported the direct manipulation of the Néel vectors by spin-orbit torque switching, offering potential pathways to directly read and write the AFM moments by all-electrical means [6–12]. However, several reports have also shown that the distinct stagger-like electrical signals may not solely originate from spin-orbit torque switching of Néel vectors, and may be contaminated by the signals from the anisotropic thermal gradient, the electromigration by the high current density, the film inhomogeneity, the magnetoelastic stress, and even the unintended consequences of the multiterminal patterned structures [13–18]. It is essential to observe the electrical signals caused solely by the antiferromagnetic Néel vectors switching.

Thus, we study the electrical signals for the uniaxial AFM Cr_2O_3, which has well-established sharp Néel vectors switching during the spin-flop transition. We reveal the *coherent* Néel vector rotation through both transverse and longitudinal resistance measurements, and we observe a symmetric Hall signal under an out-of-plane magnetic field and an angular-dependent magnetoresistance with a fourfold or plateau behavior. Furthermore, we find the Néel vector of Cr_2O_3 can be arbitrarily manipulated in plane with a small in-plane magnetic field when the magnetocrystalline anisotropy is compensated.

II. RESULTS AND DISCUSSIONS

A. Magnetic probes

The uniaxial antiferromagnetic insulator studied in our work is a single crystalline slab Cr_2O_3 (see Appendix). It has a hexagonal crystalline structure with an easy axis along the (0001) direction (parallel to the z axis), as shown in Fig. 1(a). We first confirm the spin-flop transition by a superconducting quantum interference device. By applying a magnetic field $\boldsymbol{H}$ along the easy axis (0001) of Cr_2O_3 at 10 K, as shown in Fig. 1(b) (red curve), a drastic change of the magnetization is observed at about 5.8 T due to the spin-flop transition [19,20]. Thus, the spin-flop field for Cr_2O_3 is $\boldsymbol{H}_{\text{SF}} = 5.8\,\text{T}$. Below $\boldsymbol{H}_{\text{SF}}$ ($\boldsymbol{H} < \boldsymbol{H}_{\text{SF}}$), Néel vectors maintain along the easy axis (0001), exhibiting negligible magnetization. When $\boldsymbol{H}$ reaches upon $\boldsymbol{H}_{\text{SF}}$ ($\boldsymbol{H}_z = \boldsymbol{H}_{\text{SF}}$), Néel vectors immediately flop perpendicular to (0001) and lie in the xy plane. The finite magnetization is caused by the slight tilting of the Cr_2O_3 spins towards $\boldsymbol{H}$. As $\boldsymbol{H}$ keeps increasing ($\boldsymbol{H} > \boldsymbol{H}_{\text{SF}}$), spins in both sublattices tilt towards and finally align with $\boldsymbol{H}$. In contrast, when $\boldsymbol{H}$ is applied along the hard axis ($11\bar{2}0$) or ($\bar{1}100$), no spin-flop transition occurs; only a linear change in magnetization caused by the spin tilting towards the magnetic field is observed, as shown in Fig. 1(b) (blue and green curves).

From the molecular field theory, the spin-flop field H_{SF} is determined as [21]

$$H_{\text{SF}} = \sqrt{H_A(2H_E - H_A)}, \tag{1}$$

---

*These authors contributed equally to this work.
†danru@ntu.edu.tw
‡syhuang@phys.ntu.edu.tw

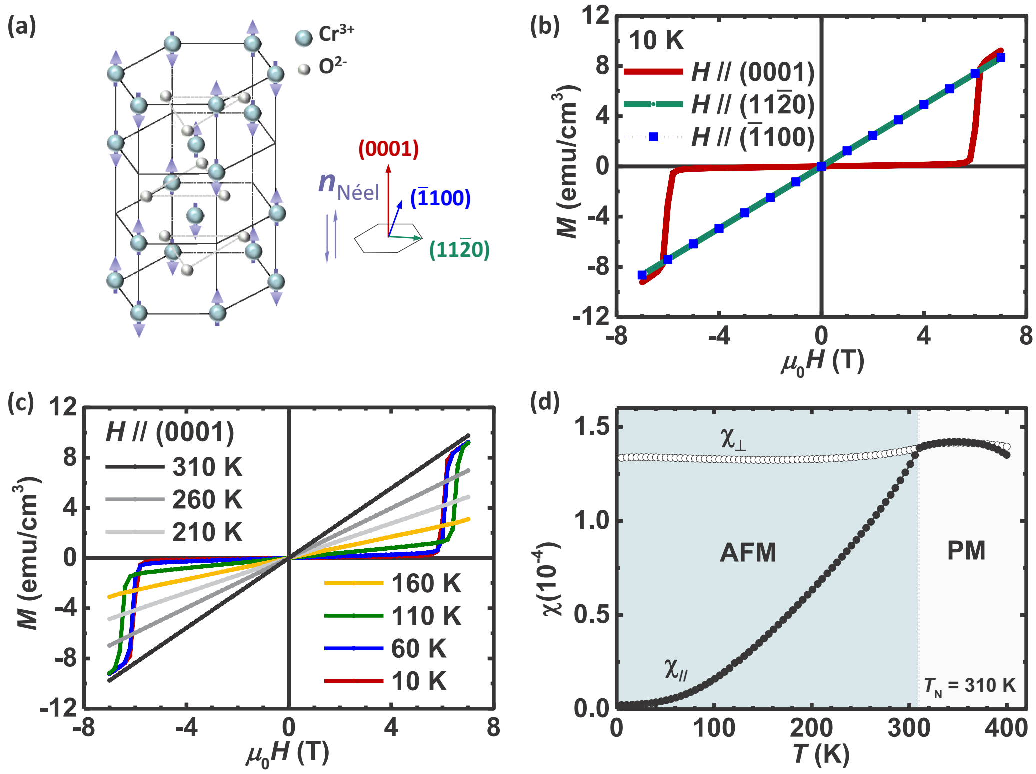

FIG. 1. Crystal structure and spin-flop transition confirmed by magnetometry for Cr_2O_3. (a) The crystal structure of Cr_2O_3. Arrows represent the Cr^{3+} spins. (b) ***M-H*** loops with magnetic field applied along the (0001) (red curve), $(11\bar{2}0)$ (green curve), and $(\bar{1}100)$ (blue dotted curve) directions. (c) Temperature-dependent ***M-H*** loops with magnetic field applied along easy axis (0001). (d) Magnetic susceptibility χ of Cr_2O_3, where $\chi_\perp$ refers to external magnetic field $\boldsymbol{H}$ perpendicular to easy axis (0001), and $\chi_\parallel$ refers to external magnetic field $\boldsymbol{H}$ parallel to easy axis (0001).

where H_A is the crystal anisotropy effective field, and H_E is the antiferromagnetic exchange coupling effective field. For Cr_2O_3, $H_A = 700\,\text{Oe}$, $H_E = 245\,\text{T}$ [22], and thus H_{SF} is estimated as 5.8 T, consistent with our experiment. In addition, from the equation

$$H_S = 2H_E - H_A \tag{2}$$

we estimate the saturation field $H_S = 490\,\text{T}$, indicating that only with such high magnetic field strength, can spins from both sublattices be completely aligned with the external magnetic field. Therefore, the robustness against external fields makes the manipulation of Néel vectors in Cr_2O_3 extremely difficult.

Besides 10 K, we also observe spin flop at different temperatures. As shown in Fig. 1(c), at 60 K, both the slope of the ***M-H*** curve at low fields and the value of $\boldsymbol{H}_{\text{SF}}$ are slightly larger than those at 10 K. At 110 K, these changes are more drastic. Above 160 K, due to the field limitation of our magnetometer (± 7 T), we no longer capture the spin-flop transition, as they shift to much higher fields. When the temperature increases up to the Néel temperature $T_N \sim 310\,\text{K}$, AFM Cr_2O_3 transits to the paramagnetic state, and thus the ***M-H*** curve is linear. The T_N for Cr_2O_3 is also confirmed by the temperature-dependent susceptibility of Cr_2O_3, as shown in Fig. 1(d). The discontinuity of the first derivative of susceptibility at 310 K marks the T_N of Cr_2O_3 [22,23]. In the region $T < T_N$, perpendicular susceptibility $\chi_\perp$ ($\boldsymbol{n}_{\text{Néel}} \perp \boldsymbol{H}$) of Cr_2O_3 is almost temperature independent, while the parallel susceptibility $\chi_\parallel$ ($\boldsymbol{n}_{\text{Néel}} \parallel \boldsymbol{H}$) increases as the temperature rises owing to the increase of thermal fluctuation. We find $\chi_\perp$ is always larger than $\chi_\parallel$. These behaviors corroborate the change of the ***M-H*** slopes in Fig. 1(c) and are well explained by the molecular field theory [19,20]. Therefore, using the magnetometer, we reveal the behavior of Cr_2O_3 Néel vectors throughout its spin-flop transition.

B. Electrical probes: Transverse resistance

To probe the coherent switching of the Néel vector electrically, we deposit a 5-nm-thick Pt film on a (0001)-orientated Cr_2O_3 single-crystal slab by DC sputtering and then pattern it into 10-μm-wide Hall bars using photolithography. The chamber has a base pressure better than 5×10^{-7} torr. The sputtering power is 20 W and the working Ar pressure is 4 mTorr with a flow rate of 30 SCCM (SCCM denotes cubic centimeter per minute at STP). The resistivity of Pt with Hall bar is $28.6\,\mu\Omega\,\text{cm}$ at 10 K and $41.7\,\mu\Omega\,\text{cm}$ at 310 K. Due to the spin Hall effect [24,25], a spin current with spin index $\boldsymbol{\sigma}$ along the $-y$ direction is generated in Pt. We first adopt the Hall effect measurement to detect the coherent $\boldsymbol{n}_{\text{Néel}}$ rotation. The measurement setup is shown in Fig. 2(a), where a constant current of 1 mA amplitude is applied along the x

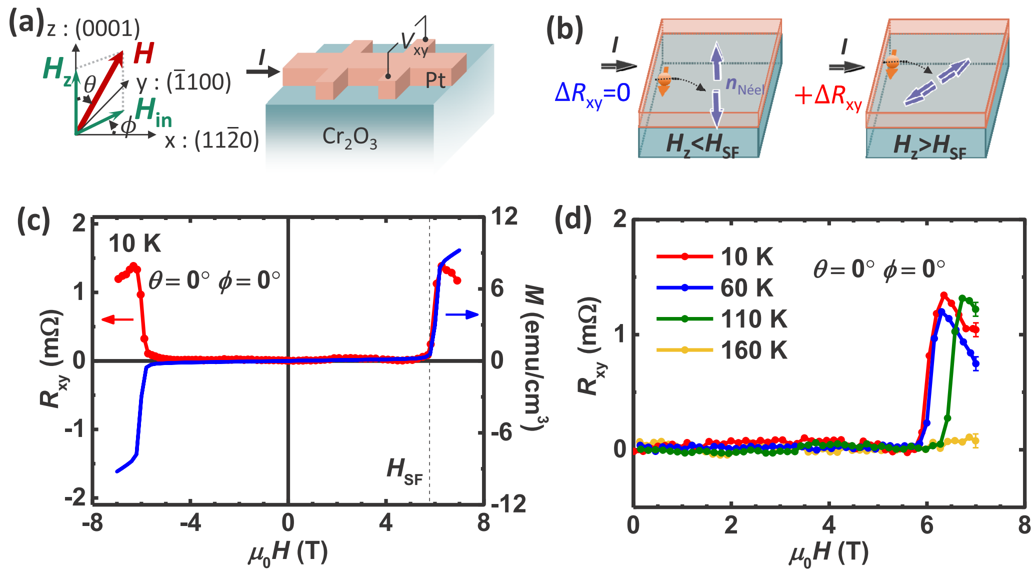

FIG. 2. Probe the coherent Néel vector switching by spin Hall planar Hall effect measurement. (a) Schematic diagram of Hall resistance R_{xy} measurement. A 5-nm-thick Pt film is deposited on the (0001)-orientated single-crystal Cr_2O_3 slab and patterned into Hall bar structure. The electrical current is applied along the (11$\bar{2}$0) direction, and the voltage V_{xy} is detected along the ($\bar{1}$100) direction. The external magnetic field $\boldsymbol{H}$ is applied along the (0001) direction. The angle between $\boldsymbol{H}$ and the z axis is θ. The angle between the magnetic field in-plane component $\boldsymbol{H}_{\rm in}$ and the x axis is ϕ. (b) The spin current (orange arrow) generated in Pt is utilized to probe the orientations of Néel vectors (blue arrows) in Cr_2O_3. For Cr_2O_3 samples with $\boldsymbol{n}_{\rm Néel}$ perpendicular and rotated 45° positively against the x axis, the transverse resistances R_{xy} of Pt exhibit zero and positive finite values, respectively. (c) Field-dependent Hall resistance R_{xy} at 10 K after subtracting the negative linear ordinary Hall background. (d) Field-dependent R_{xy} under various temperatures, including 10, 60, 110, and 160 K.

axis (11$\bar{2}$0), and the induced voltage is detected along the y axis ($\bar{1}$100). We sweep the external magnetic field $\boldsymbol{H}$ from +7 to −7 T and reversely along the (0001) direction with $\theta = 0°$. We define the angle between $\boldsymbol{H}$ and the z axis as θ and that between the $\boldsymbol{H}$ in-plane projection and the x axis as ϕ. After subtracting the negative linear ordinary Hall background (see Appendix), we replot the Hall resistance R_{xy} in Fig. 2(c) (red curve). We observe a resistance "jump" in the Hall signal. Notably, the observed Hall signal is symmetric in the field, in sharp contrast to the asymmetric ones often seen in Hall effect measurements with the out-of-plane magnetic field. For comparison, we put the ***M-H*** loop (blue curve) in the same graph. It is clear that the resistance "jump" field and spin-flop field $\boldsymbol{H}_{\rm SF}$ are consistent with each other, indicating the same origin. The symmetric R_{xy} signal can be understood from the spin Hall planar Hall effect (we use PHE for simplification), where $\boldsymbol{n}_{\rm Néel}$ experiences a coherent rotation of 90° from (0001) to the xy plane and is detected by pure spin current from Pt. As shown in Fig. 2(b), when $|\boldsymbol{H}_z| < |\boldsymbol{H}_{\rm SF}|$, $\boldsymbol{n}_{\rm Néel}$ is along the easy axis (0001), perpendicular to $\boldsymbol{\sigma}$, contributing zero Hall resistance. When $|\boldsymbol{H}_z| > |\boldsymbol{H}_{\rm SF}|$, $\boldsymbol{n}_{\rm Néel}$ flops onto the xy plane, forming an angle with spin index $\boldsymbol{\sigma}$, and when the angle is not 0° or 90°, there is a nonzero PHE resistance. Thus, the sizable symmetric Hall signal is attributed to PHE. We further vary the temperature from 10 to 160 K, as shown in Fig. 2(d). We find the resistance jump field increases with increasing temperature, corresponding to the spin-flop field at each temperature determined by the magnetometer. From these results, we verify that the PHE is an important and reliable tool to probe the coherent switching of the antiferromagnetic Néel vector electrically.

C. Electrical probes: Longitudinal resistance

We then study the coherent $\boldsymbol{n}_{\rm Néel}$ rotation by the longitudinal resistance. The measurement setup is shown in Fig. 3(a), where a current of 1 mA is applied along the x axis (11$\bar{2}$0), and the induced voltage is detected in the same direction. We sweep the external magnetic field $\boldsymbol{H}$ from +7 to −7 T and reversely along the (0001) and (11$\bar{2}$0) directions with $\theta = 0°$ and 90°, respectively, and $\phi = 0°$. We define the angle between the magnetic field in-plane component and the x axis as ϕ. When the antiferromagnetic $\boldsymbol{n}_{\rm Néel}$ is parallel with or perpendicular to $\boldsymbol{\sigma}$, the longitudinal resistance is small or large, respectively, according to the spin Hall magnetoresistance [26–28]. We subtract the longitudinal resistances obtained at various fields $R_{xx}(H)$ with R_{xx} at $H = 0$ T and present our results as ΔR_{xx}. As shown in Fig. 3(b) (red solid circle curve), when $\boldsymbol{H}$ is along the easy axis (0001) and is smaller than $H_{\rm SF}$, R_{xx} increases almost linearly with $\boldsymbol{H}$, due to the interplay between ordinary magnetoresistance (OMR) [29] and weak localization [30–32]. When $\boldsymbol{H} > \boldsymbol{H}_{\rm SF}$, R_{xx} drastically drops. This is due to the sudden change in the relative direction between spin index $\boldsymbol{\sigma}$ and Néel vector $\boldsymbol{n}_{\rm Néel}$ from perpendicular to parallel. In comparison, when the magnetic field is applied along the hard axis (11$\bar{2}$0), only OMR proportional to H^2 is observed in Fig. 3(b) (red open circle curve), where spins in both sublattices of $\boldsymbol{n}_{\rm Néel}$ slightly and linearly tilt towards $\boldsymbol{H}$. The spin Hall magnetoresistance measurement further corroborates the electrical detection of the antiferromagnetic $\boldsymbol{n}_{\rm Néel}$ coherent switching. Note that the parabolic and linear field dependence is not the evidence for Néel vector rotation, but solely caused

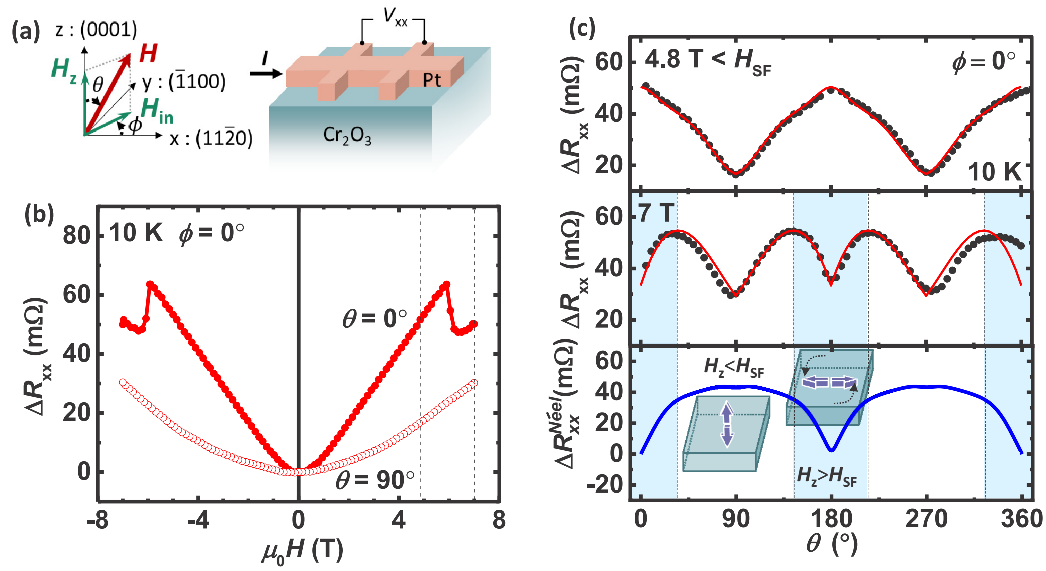

FIG. 3. Probe of the coherent Néel vector switching by spin Hall magnetoresistance measurement. (a) Schematic diagram of the spin Hall magnetoresistance R_{xx} measurement, where the electrical current and detected voltage are both along the x axis $(11\bar{2}0)$. The external magnetic field $\boldsymbol{H}$ is tilted with a small angle θ away from the z axis and ϕ away from the x axis. (b) Longitudinal magnetoresistance R_{xx} when $\boldsymbol{H}$ is along the easy axis (0001) at $\theta = 0^\circ$ (solid circle) and along the hard axis $(11\bar{2}0)$ at $\theta = 90^\circ$ (open circle). We subtract R_{xx} obtained at $H = 0\,\mathrm{T}$ from the longitudinal resistances obtained at various fields $R_{xx}(\boldsymbol{H})$ and present our results as ΔR_{xx}. (c) The magnetic field angular dependence of the longitudinal magnetoresistance with $\boldsymbol{H} = 4.8\,\mathrm{T}$ (top) and $\boldsymbol{H} = 7\,\mathrm{T}$ (middle). The bottom panel represents the angular-dependent magnetoresistance that solely comes from the Néel vector rotation and we present the data as $\Delta R_{xx}^{\mathrm{Néel}}$. This is realized by subtracting the estimated angular-dependent OMR from the experimentally obtained angular-dependent R_{xx} at $\boldsymbol{H} = 7\,\mathrm{T}$. To clearly demonstrate the change of resistance due to Néel vector rotation, $\Delta R_{xx}^{\mathrm{Néel}}$ is vertically shifted.

by the ordinary magnetoresistance and weak localization in Pt.

Another way to distinguish the contribution between $\boldsymbol{n}_{\mathrm{Néel}}$ coherent switching and OMR is through the angular dependence of the MR. We rotate magnetic fields in the xz plane with θ varying from 0° to 360°. When $\boldsymbol{H} = 4.8\,\mathrm{T} < \boldsymbol{H}_{\mathrm{SF}}$, we observe an angular dependence of $\cos^2\theta$, as shown in Fig. 3(c) (top), which is entirely caused by OMR in Pt because $\boldsymbol{n}_{\mathrm{Néel}}$ is nearly unchanged before the spin-flop transition. It is clear that the $\cos^2\theta$ behavior in our study is not the evidence for antiferromagnetic $\boldsymbol{n}_{\mathrm{Néel}}$ rotation from previous reports [17,26,33–35].

When $\boldsymbol{H} = 7\,\mathrm{T} > \boldsymbol{H}_{\mathrm{SF}}$, we observe a drastically different *fourfold* curve, as shown in Fig. 3(c) (middle). Here, we discuss the possible origin of the angular dependence of R_{xx} between $\theta = 0^\circ$ to 90°, and results in the region of $\theta > 90^\circ$ can be understood similarly. When $\theta = 0^\circ$, the out-of-plane magnetic field component of $\boldsymbol{H}_z = 7\,\mathrm{T}$ fulfills the spin-flop condition, with $\boldsymbol{n}_{\mathrm{Néel}}$ parallel with $\boldsymbol{\sigma}$ along the y axis, corresponding to the minimum R_{xx}. As θ increases, $\boldsymbol{H}_z$ reduces, and the in-plane component $\boldsymbol{H}_{\mathrm{in}}$ increases. Thus, spins in $\boldsymbol{n}_{\mathrm{Néel}}$ are tilted away from the y axis, resulting in the increase of R_{xx}. When $\theta = 35^\circ$, $\boldsymbol{H}_z$ is below $\boldsymbol{H}_{\mathrm{SF}}$ and spins in $\boldsymbol{n}_{\mathrm{Néel}}$ are mainly aligned back to the easy axis (z axis), with minor tilting along the x axis, corresponding to the maximum R_{xx}. As θ further increases to 90°, $\boldsymbol{H}_x$ increases, and both spins in $\boldsymbol{n}_{\mathrm{Néel}}$ are tilting from the z axis towards the x axis. Since $\boldsymbol{\sigma}$ is along the y axis, the R_{xx} caused by $\boldsymbol{n}_{\mathrm{Néel}}$ rotation in the xz plane is the same. Thus, R_{xx} is expected to stay unchanged between 35° and 90°. But Fig. 3(c) (middle) shows a much more complicated behavior due to a mixture of OMR and spin Hall magnetoresistance (SMR). By subtracting the expected OMR contribution at 7 T, we obtain a spin-dependent signal $\Delta R_{xx}^{\mathrm{Néel}}$ that solely comes from $\boldsymbol{n}_{\mathrm{Néel}}$ rotation in Fig. 3(c) (bottom). Note that the OMR at 7 T is extrapolated from the result at 4.8 T in the top panel of Fig. 3(c) by using the H^2 relation. We mark $\theta < 35^\circ$ as the blue region, where $\boldsymbol{H}_z > \boldsymbol{H}_{\mathrm{SF}}$. We mark $35^\circ < \theta < 90^\circ$ as the "white region," where $H_z < H_{\mathrm{SF}}$ and SMR in this region shows a plateau behavior as expected since the magnetic field component along the easy axis no longer supports the coherent switching of $\boldsymbol{n}_{\mathrm{Néel}}$. Thus, we demonstrate the angular-dependent magnetoresistance R_{xx} for antiferromagnetic systems that experience the coherent $\boldsymbol{n}_{\mathrm{Néel}}$ rotation.

Additionally, when we rotate magnetic fields in the xy or yz plane with θ varying from 0° to 360°, the angular-dependent resistance shows $\cos^2\theta$ angular dependence (see Appendix), which mainly comes from the OMR contribution from Pt. These results are in sharp contrast to the fourfold or plateau behavior that captures the coherent rotation of $\boldsymbol{n}_{\mathrm{Néel}}$.

D. Manipulation of $\boldsymbol{n}_{\mathrm{Néel}}$

Beyond the electrical detection of the coherent rotation of $\boldsymbol{n}_{\mathrm{Néel}}$, we also demonstrate the manipulation of the $\boldsymbol{n}_{\mathrm{Néel}}$ with a small in-plane magnetic field when the magnetocrystalline anisotropy energy is compensated by the Zeeman energy. It is well known that the $\boldsymbol{n}_{\mathrm{Néel}}$ flops onto the plane perpendicular to the easy axis after the spin-flop transition, but less is known on which axis the $\boldsymbol{n}_{\mathrm{Néel}}$ is aligned with. We propose a physical picture to describe the behavior of $\boldsymbol{n}_{\mathrm{Néel}}$ after the spin-flop transition, where the $\boldsymbol{n}_{\mathrm{Néel}}$ is perpendicular to the in-plane

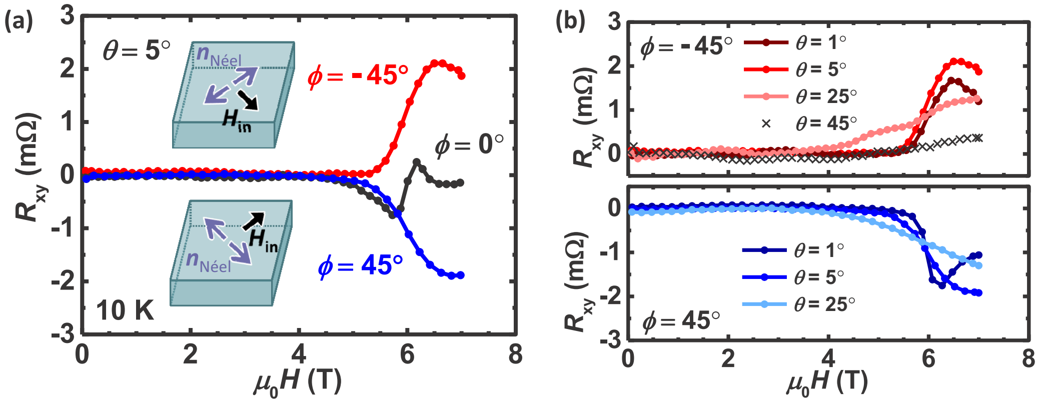

FIG. 4. Probe the coherent Néel vector switching with various θ and ϕ angles. (a) Field-dependent R_{xy} with $\boldsymbol{H} = 7\,\mathrm{T}$ tilting at $\theta = 5^\circ$ and $\boldsymbol{H}_{\text{in}} = 6100\,\mathrm{Oe}$ modulating along $\phi = -45^\circ$ (red curve), 0° (black curve), and $+45^\circ$ (blue curve). (b) Field-dependent R_{xy} with $\theta = 1^\circ$ (dark-red/blue), 5° (red/blue), 25° (light-red/blue), and 45° (crosses) and $\phi = -45^\circ$ (red curves), and $+45^\circ$ (blue curves).

magnetic field $\boldsymbol{H}_{\text{in}}$ due to the lowest Zeeman energy. Experimentally, we intentionally tilt the external magnetic field $\boldsymbol{H}$ with a small angle θ away from the z axis. The $\boldsymbol{H}$ projected in the xy plane is $\boldsymbol{H}_{\text{in}}$. In this case, $\boldsymbol{H}_z$ is still larger than $\boldsymbol{H}_{\text{SF}}$; meanwhile, there is an additional in-plane component $\boldsymbol{H}_{\text{in}}$. We define the angle between $\boldsymbol{H}_{\text{in}}$ and the x axis as ϕ. Thus, when $\phi = -45^\circ$, $\boldsymbol{n}_{\text{Néel}}$ is 45° with respect to the x axis, contributing positive R_{xy}. Similarly, when $\phi = +45^\circ$, R_{xy} is negative. As shown in Fig. 4(a), by tilting $\boldsymbol{H} = 7\,\mathrm{T}$ with $\theta = 5^\circ$, we have $H_z = 6.97\,\mathrm{T} > H_{\text{SF}} = 5.8\,\mathrm{T}$ and $H_{\text{in}} = 6100\,\mathrm{Oe}$. We modulate $\boldsymbol{H}_{\text{in}}$ along $\phi = -45^\circ$ and $+45^\circ$, and we observe the positive (red curve) and negative (blue curve) R_{xy}, respectively. When $\phi = 0^\circ$, $\boldsymbol{n}_{\text{Néel}}$ is parallel with spin index $\boldsymbol{\sigma}$, contributing zero R_{xy} except for slight fluctuation during the spin-flop transition (black curve). Therefore, we demonstrate a scheme to manipulate the $\boldsymbol{n}_{\text{Néel}}$ with an in-plane magnetic field when the magnetocrystalline anisotropy is compensated.

In addition to $\theta = 5^\circ$, we also study $\theta = 1^\circ$, 25°, and 45°. With $\theta = 1^\circ$, the in-plane component $\boldsymbol{H}_{\text{in}}$ is only about 1200 Oe. The two reversed signals (brown and dark-blue curves) in Fig. 4(b) indicate that the Néel vector can still be manipulated by $\boldsymbol{H}_{\text{in}}$. However, when the tilted angle θ is increased to 25°, in which the z-axis component $\boldsymbol{H}_z$ could only reach 6.34 T, barely satisfying spin-flop condition, the process of Néel vector rotation is prolonged (light-red and light-blue curves). When θ increases to 45°, in which the maximum z-component magnetic field $\boldsymbol{H}_z$ is 4.95 T, lower than the $\boldsymbol{H}_{\text{SF}} = 5.8\,\mathrm{T}$, we could not observe a significant Hall signal (black crosses), indicating the Néel vectors can be hardly manipulated. Those results verify the manipulation of the Néel vector by a small in-plane magnetic field when the magnetocrystalline anisotropy is compensated by Zeeman energy.

III. CONCLUSIONS

The detection and manipulation of Néel vectors have been both an excitement and a challenge during the past few years. In this work, through the spin-flop transition in Cr_2O_3, we observe the pure electrical signal from Néel vector switching and demonstrate the electrical detection and manipulation of the antiferromagnetic Néel vector. We report a symmetric Hall signal under an out-of-plane magnetic field and an angular-dependent magnetoresistance with a fourfold or plateau behavior. Furthermore, we successfully manipulate the Néel vector by an in-plane magnetic field when the magnetocrystalline anisotropy energy is compensated. It is worth pointing out, although we detect the Néel vectors in bulk Cr_2O_3, the electrical detection method using the spin Hall/planar Hall magnetoresistance can be also effective for antiferromagnetic thin films. Reports have shown that the spin-flop transition behaviors are similar for Cr_2O_3 bulks and thin films [36,37]. By using the same experimental technique, we also successfully detect the Néel vector switching in Cr_2O_3 thin films. These results will be published separately. Comparing with previous works that study the Cr_2O_3 thin films with scanning magnetic field lower than the spin-flop field [33,34], our work with magnetic field up to 7 T demonstrates clearly the electrical detection of the spin-flop transition and thus the Néel vector rotation in Cr_2O_3. Our work provides significant insights for exploiting Néel vectors in antiferromagnetic materials and has the potential to achieve ultrafast, high-density, and low-power consuming AFM-based spintronic devices.

ACKNOWLEDGMENTS

This work is financially supported by the Ministry of Science and Technology of Taiwan under Grant No. MOST 109-2123-M-002-002, No. MOST 110-2112-M-002-047-MY3 and the Center of Atomic Initiative for New Materials (AI-Mat), National Taiwan University, Taipei, Taiwan from the Featured Areas Research Center Program within the framework of the Higher Education Sprout Project by the Ministry of Education (MOE) in Taiwan.

APPENDIX

1. Characterization of the single-crystal Cr_2O_3 slab

The uniaxial antiferromagnetic insulator Cr_2O_3 studied in our work is a single crystalline slab with dimensions of $5 \times 5 \times 0.5\,\mathrm{mm}^3$ obtained from SurfaceNet GmbH. It has a hexagonal crystalline structure with an easy axis along the (0001) direction. The x-ray diffraction (XRD) patterns in Fig. 5(a) exhibit sharp (0006) and (00012) peaks at $2\theta = 39.7^\circ$ and $2\theta = 85.7^\circ$ over a broad range of 2θ, confirming

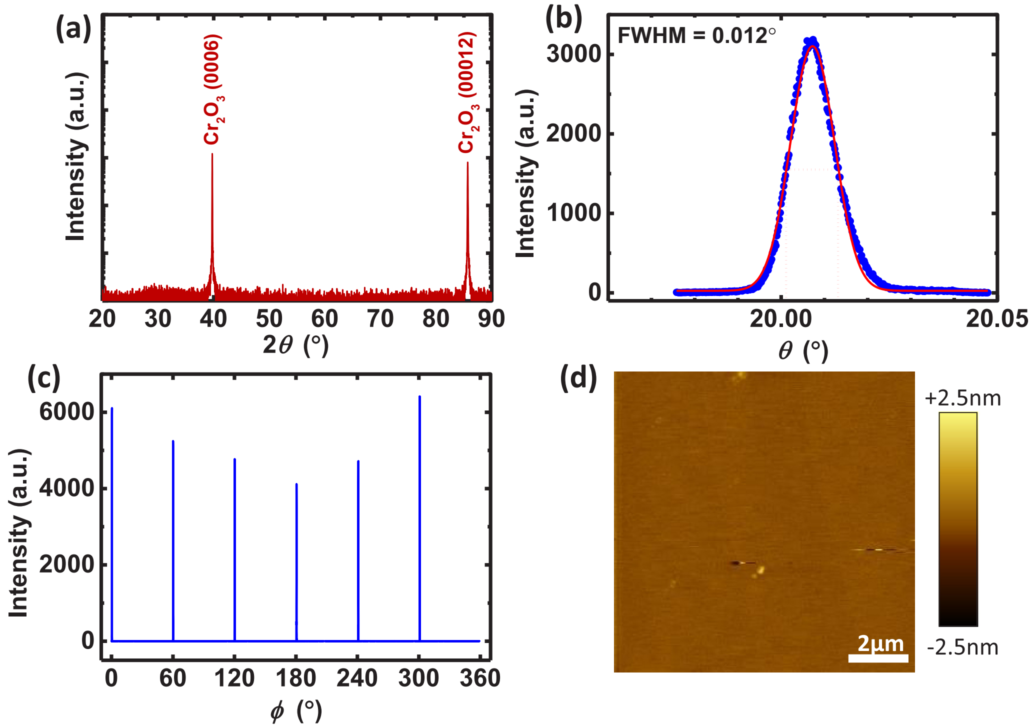

FIG. 5. Characterization of single-crystal Cr_2O_3 slab. (a) 2θ XRD pattern of (0001) single-crystal Cr_2O_3 slab. (b) Rocking curve of (0006) peak with FWHM $= 0.012^\circ$ indicates a high crystallinity of single-crystal Cr_2O_3 slab. (c) ϕ-scan result with sixfold symmetry ensures the pure orientation of single-crystal Cr_2O_3 slab. (d) (0001) single-crystal Cr_2O_3 slab surface morphology taken by atomic force microscope.

a pure (0001) orientation. The rocking curve shows narrow full width at half maximum (FWHM) of 0.012. The sixfold symmetry in ϕ scan further ensures the high crystallinity of the slab, as shown in Figs. 5(b) and 5(c). The surface morphology over a 1010 μm^2 area taken by an atomic force microscope exhibits a root-mean-square roughness about 0.1 nm, indicating a smooth surface, as shown in Fig. 5(d).

2. Spin-flop transition

For a uniaxial AFM, when there is no magnetic field, the Néel vectors prefer to lie in the easy axis, e.g., along the (0001) direction. When a small magnetic field is applied along the easy axis, the Néel vectors remain nearly unchanged due to the enormous exchange coupling and crystalline anisotropy, as shown in Fig. 6(a). However, when the magnetic field is large enough to overcome the pining of the crystalline anisotropy, Néel vectors suddenly flop perpendicular to the easy axis, as shown in Fig. 6(b). This process is called spin-flop transition [19,20]. As the field continues to increase, both spins in the sublattices of the Néel vectors tilt towards and finally align with the magnetic field, as shown in Fig. 6(c). In contrast, when the magnetic field is applied perpendicular to the easy axis, the Néel vectors do not experience the spin-flop transition, but spins in both sublattices tilt towards the field direction as the field amplitude increases, as shown in Fig. 6(d).

3. Electrical detection

To electrically probe the Néel vectors in the antiferromagnetic insulator, we utilize the spin current generated from the attached metallic layer. Due to the spin Hall effect, a spin current is generated in Pt, flowing perpendicular to the interface, and is reflected or absorbed by the magnetic materials in the vicinity. The reflected spin current is then converted back to

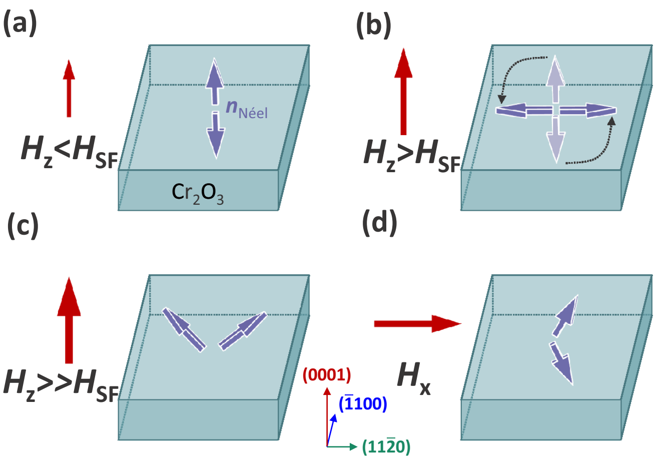

FIG. 6. Schematic diagram for the spin-flop transition in Cr_2O_3 and the electrical detection of its Néel vector $\boldsymbol{n}_{\text{Néel}}$. (a) Néel vector $\boldsymbol{n}_{\text{Néel}}$ (blue arrows) of Cr_2O_3 stands along easy axis (0001) when $H_z < H_{SF}$. (b) Néel vector $\boldsymbol{n}_{\text{Néel}}$ of Cr_2O_3 suddenly flops onto the plane perpendicular to the easy axis when $H_z > H_{SF}$. (c) When H_z continues to increase, spins in both sublattices of the Néel vector tilt towards and finally align with the magnetic field. (d) When the magnetic field H_x is applied along the hard axis $(11\bar{2}0)$, spins in $\boldsymbol{n}_{\text{Néel}}$ tilt towards and finally align with the field.

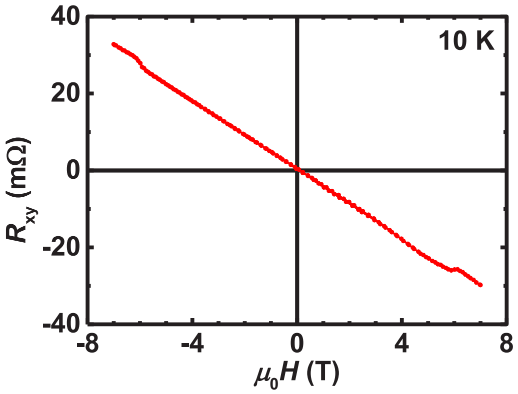

FIG. 7. Raw data of field-dependent Hall resistance at 10 K.

charge current through the inverse spin Hall effect, resulting in changes in the Pt resistance. The amount of spin current being reflected or absorbed depends on the angle between the Néel vector $\boldsymbol{n}_{\text{Néel}}$ (blue arrows) and the spin index $\boldsymbol{\sigma}$ (yellow arrow). The maximum absorption and reflection occur when $\boldsymbol{n}_{\text{Néel}}$ is perpendicular ($\boldsymbol{n}_{\text{Néel}} \perp \boldsymbol{\sigma}$) and parallel to $\boldsymbol{\sigma}$ ($\boldsymbol{n}_{\text{Néel}} \parallel \boldsymbol{\sigma}$), respectively, generating maximum and minimum longitudinal resistance in Pt [26]. This is also known as the SMR [27]. Meanwhile, the transverse Hall resistance is maximized and minimized with the opposite signs when $\boldsymbol{n}_{\text{Néel}}$ is -45° and $+45^\circ$ angled with $\boldsymbol{\sigma}$, respectively, in the film plane [28]. This is the spin Hall PHE. Thus, from the change of the SMR and PHE signal in Pt, one detects the direction of $\boldsymbol{n}_{\text{Néel}}$ in the antiferromagnetic insulator layer.

4. Field-dependent Hall resistance

In Fig. 7, we show the raw data for the field-dependent Hall resistance R_{xy} at 10 K. The negative-slope linear background comes from the ordinary Hall effect of the Pt layer. A symmetric jump signal happens at spin-flop field $\boldsymbol{H}_{\text{SF}}$.

5. Spin Hall magnetoresistance with magnetic field along various directions

When we rotate magnetic fields in the xy or yz plane with θ varying from 0° to 360°, the angular-dependent resistance is completely different from that in the xz plane. As shown in Fig. 8(a), in the hard axis measurement with accessible H_x and H_y, $\boldsymbol{n}_{\text{Néel}}$ stays nearly unperturbed along the z axis, with no spin-flop transition in the field-dependent R_{xx} measurements, in sharp contrast to the situation with $\boldsymbol{H}$ along the easy axis in Fig. 8(c). Also, in the xy field angular scan, as shown in Fig. 8(b), a $\cos^2\phi$ signal is captured, which mainly comes from OMR due to the lack of spin-flop transition. In the yz-plane field angular scan, as shown in Fig. 8(d), before and after spin flop at $\boldsymbol{H} = 4.8$ T and $\boldsymbol{H} = 7$ T, respectively, the relative direction between spin index $\boldsymbol{\sigma}$ and Néel vector $\boldsymbol{n}_{\text{Néel}}$ remain perpendicular. Therefore, both curves have the same $\cos^2\theta$ angular dependence, which mainly comes from OMR contribution. This result is in sharp contrast to the fourfold or plateau behavior discussed earlier, which provides evidence of the spin-dependent electrical responses of coherent rotation of $\boldsymbol{n}_{\text{Néel}}$.

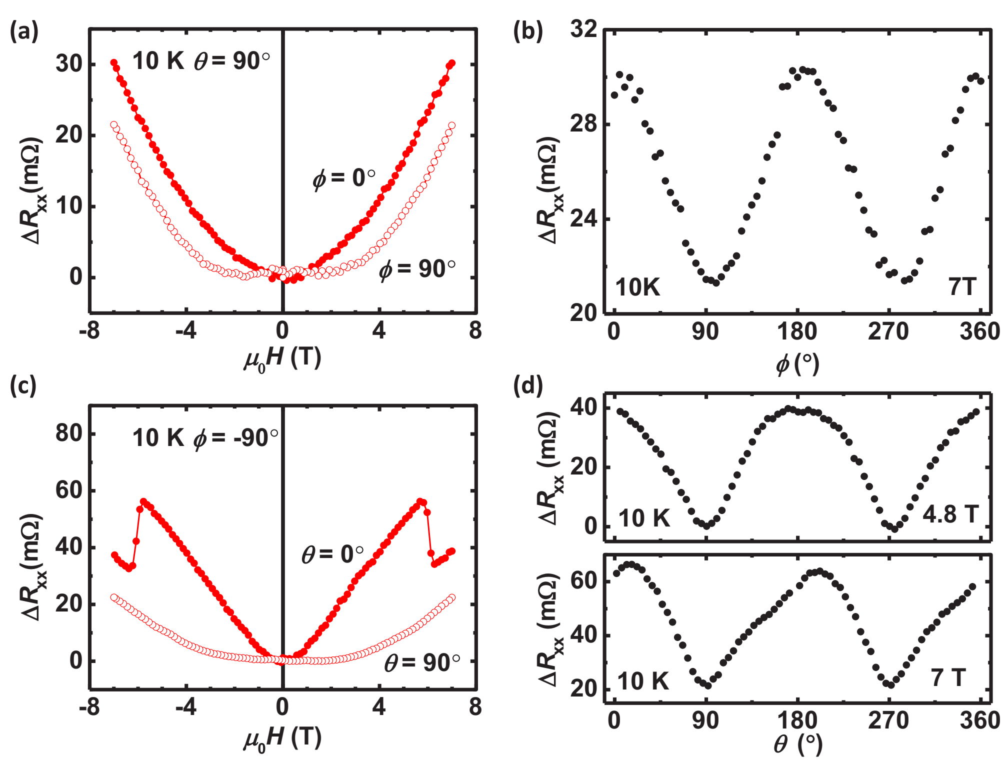

FIG. 8. Spin Hall magnetoresistance with magnetic field in various directions. (a) R_{xx}-H with H along the x (solid circle) and y (open circle) axes. (b) Magnetic field angular scan with H rotating in the xy plane. (c) R_{xx}-H with H along the z (solid circle) and y (open circle) axes. (d) Magnetic field angular scan with H rotating in the yz plane, below (top) and above (bottom) the spin-flop field.

[1] L. Néel, Magnetism and local molecular field, Science **174**, 985 (1971).

[2] V. Baltz, A. Manchon, M. Tsoi, T. Moriyama, T. Ono, and Y. Tserkovnyak, Antiferromagnetic spintronics, Rev. Mod. Phys. **90**, 015005 (2018).

[3] J. Železný, P. Wadley, K. Olejník, A. Hoffmann, and H. Ohno, Spin transport and spin torque in antiferromagnetic devices, Nat. Phys. **14**, 220 (2018).

[4] A. Manchon, J. Železný, I. M. Miron, T. Jungwirth, J. Sinova, A. Thiaville, K. Garello, and P. Gambardella, Current-induced spin-orbit torques in ferromagnetic and antiferromagnetic systems, Rev. Mod. Phys. **91**, 035004 (2019).

[5] X. Marti, I. Fina, C. Frontera, J. Liu, P. Wadley, Q. He, R. J. Paull, J. D. Clarkson, J. Kudrnovsky, I. Turek, J. Kuneš, D. Yi, J. H. Chu, C. T. Nelson, L. You, E. Arenholz, S. Salahuddin, J. Fontcuberta, T. Jungwirth, and R. Ramesh, Room-temperature antiferromagnetic memory resistor, Nat. Mater. **13**, 367 (2014).

[6] P. Wadley, B. Howells, J. Železný, C. Andrews, V. Hills, R. P. Campion, V. Novák, K. Olejník, F. Maccherozzi, S. S. Dhesi, S. Y. Martin, T. Wagner, J. Wunderlich, F. Freimuth, Y. Mokrousov, J. Kuneš, J. S. Chauhan, M. J. Grzybowski, A. W. Rushforth, K. W. Edmonds, B. L. Gallagher, and T. Jungwirth, Electrical switching of an antiferromagnet, Science **351**, 587 (2016).

[7] X. Z. Chen, R. Zarzuela, J. Zhang, C. Song, X. F. Zhou, G. Y. Shi, F. Li, H. A. Zhou, W. J. Jiang, F. Pan, and Y. Tserkovnyak, Antidamping-Torque-Induced Switching in Biaxial Antiferromagnetic Insulators, Phys. Rev. Lett. **120**, 207204 (2018).

[8] S. Y. Bodnar, L. Šmejkal, I. Turek, T. Jungwirth, O. Gomonay, J. Sinova, A. A. Sapozhnik, H. J. Elmers, M. Kläui, and M. Jourdan, Writing and reading antiferromagnetic Mn_2Au by Néel spin-orbit torques and large anisotropic magnetoresistance, Nat. Commun. **9**, 348 (2018).

[9] X. F. Zhou, J. Zhang, F. Li, X. Z. Chen, G. Y. Shi, Y. Z. Tan, Y. D. Gu, M. S. Saleem, H. Q. Wu, F. Pan, and C. Song, Strong Orientation-Dependent Spin-Orbit Torque in Thin Films of the Antiferromagnet Mn_2Au, Phys. Rev. Appl. **9**, 054028 (2018).

[10] L. Baldrati, O. Gomonay, A. Ross, M. Filianina, R. Lebrun, R. Ramos, C. Leveille, F. Fuhrmann, T. R. Forrest, F. Maccherozzi, S. Valencia, F. Kronast, E. Saitoh, J. Sinova, and M. Kläui, Mechanism of Néel Order Switching in Antiferromagnetic Thin Films Revealed by Magnetotransport and Direct Imaging, Phys. Rev. Lett. **123**, 177201 (2019).

[11] T. Moriyama, K. Oda, T. Ohkochi, M. Kimata, and T. Ono, Spin torque control of antiferromagnetic moments in NiO, Sci. Rep. **8**, 14167 (2018).

[12] L. Baldrati, C. Schmitt, O. Gomonay, R. Lebrun, R. Ramos, E. Saitoh, J. Sinova, and M. Kläui, Efficient Spin Torques in Antiferromagnetic CoO/Pt Quantified by Comparing Field- and Current-Induced Switching, Phys. Rev. Lett. **125**, 077201 (2020).

[13] C. C. Chiang, S. Y. Huang, D. Qu, P. H. Wu, and C. L. Chien, Absence of Evidence of Electrical Switching of the Antiferromagnetic Néel Vector, Phys. Rev. Lett. **123**, 227203 (2019).

[14] A. Churikova, D. Bono, B. Neltner, A. Wittmann, L. Scipioni, A. Shepard, T. Newhouse-Illige, J. Greer, and G. S. D. Beach, Non-magnetic origin of spin Hall magnetoresistance-like signals in Pt films and epitaxial NiO/Pt bilayers, Appl. Phys. Lett. **116**, 022410 (2020).

[15] T. Matalla-Wagner, J.-M. Schmalhorst, G. Reiss, N. Tamura, and M. Meinert, Resistive contribution in electrical-switching experiments with antiferromagnets, Phys. Rev. Res. **2**, 033077 (2020).

[16] P. Zhang, J. Finley, T. Safi, and L. Liu, Quantitative Study on Current-Induced Effect in an Antiferromagnet Insulator/Pt Bilayer Film, Phys. Rev. Lett. **123**, 247206 (2019).

[17] Y. Cheng, S. Yu, M. Zhu, J. Hwang, and F. Yang, Electrical Switching of Tristate Antiferromagnetic Néel Order in α-Fe_2O_3 Epitaxial Films, Phys. Rev. Lett. **124**, 027202 (2020).

[18] H. Meer, F. Schreiber, C. Schmitt, R. Ramos, E. Saitoh, O. Gomonay, J. Sinova, L. Baldrati, and M. Kläui, Direct imaging of current-induced antiferromagnetic switching revealing a pure thermomagnetoelastic switching mechanism in NiO, Nano Lett. **21**, 114 (2021).

[19] J. M. D. Coey, *Magnetism and Magnetic Materials* (Cambridge University Press, Cambridge, 2010).

[20] B. D. Cullity and C. D. Graham, *Introduction to Magnetic Materials* (Wiley-IEEE Press, Hoboken, NJ, 2008).

[21] A. G. Gurevich and G. A. Melkov, *Magnetization Oscillations and Waves* (CRC Press, Boca Raton, 1996).

[22] S. Foner, High-field antiferromagnetic resonance in Cr_2O_3, Phys. Rev. **130**, 183 (1963).

[23] E. S. Dayhoff, Antiferromagnetic resonance in Cr_2O_3, Phys. Rev. **107**, 84 (1957).

[24] Y. K. Kato, R. C. Myers, A. C. Gossard, and D. D. Awschalom, Observation of the spin Hall effect in semiconductors, Science **306**, 1910 (2004).

[25] E. Saitoh, M. Ueda, H. Miyajima, and G. Tatara, Conversion of spin current into charge current at room temperature: Inverse spin-Hall effect, Appl. Phys. Lett. **88**, 182509 (2006).

[26] G. R. Hoogeboom, A. Aqeel, T. Kuschel, T. T. M. Palstra, and B. J. van Wees, Negative spin Hall magnetoresistance of Pt on the bulk easy-plane antiferromagnet NiO, Appl. Phys. Lett. **111**, 052409 (2017).

[27] H. Nakayama, M. Althammer, Y. T. Chen, K. Uchida, Y. Kajiwara, D. Kikuchi, T. Ohtani, S. Geprägs, M. Opel, S. Takahashi, R. Gross, G. E. Bauer, S. T. Goennenwein, and E. Saitoh, Spin Hall Magnetoresistance Induced by a Nonequilibrium Proximity Effect, Phys. Rev. Lett. **110**, 206601 (2013).

[28] M. Althammer, S. Meyer, H. Nakayama, M. Schreier, S. Altmannshofer, M. Weiler, H. Huebl, S. Geprägs, M. Opel, R. Gross, D. Meier, C. Klewe, T. Kuschel, J.-M. Schmalhorst, G. Reiss, L. Shen, A. Gupta, Y.-T. Chen, G. E. W. Bauer, E. Saitoh, and S. T. B. Goennenwein, Quantitative study of the spin Hall magnetoresistance in ferromagnetic insulator/normal metal hybrids, Phys. Rev. B **87**, 224401 (2013).

[29] F. Duan and J. Guojun, *Introduction to Condensed Matter Physics* (World Scientific, Singapore, 2005).

[30] H. Z. Lu and S. Q. Shen, Finite-Temperature Conductivity and Magnetoconductivity of Topological Insulators, Phys. Rev. Lett. **112**, 146601 (2014).

[31] Y. Shiomi, T. Ohtani, S. Iguchi, T. Sasaki, Z. Qiu, H. Nakayama, K. Uchida, and E. Saitoh, Interface-dependent magnetotransport properties for thin Pt films on ferrimagnetic $Y_3Fe_5O_{12}$, Appl. Phys. Lett. **104**, 242406 (2014).

[32] B. F. Miao, S. Y. Huang, D. Qu, and C. L. Chien, Physical Origins of the New Magnetoresistance in Pt/YIG, Phys. Rev. Lett. **112**, 236601 (2014).

[33] Y. Ji, J. Miao, Y. M. Zhu, K. K. Meng, X. G. Xu, J. K. Chen, Y. Wu, and Y. Jiang, Negative spin Hall magnetoresistance in antiferromagnetic Cr_2O_3/Ta bilayer at low temperature region, Appl. Phys. Lett. **112**, 232404 (2018).

[34] R. Schlitz, T. Kosub, A. Thomas, S. Fabretti, K. Nielsch, D. Makarov, and S. T. B. Goennenwein, Evolution of the spin Hall magnetoresistance in Cr_2O_3/Pt bilayers close to the Néel temperature, Appl. Phys. Lett. **112**, 132401 (2018).

[35] L. Baldrati, A. Ross, T. Niizeki, C. Schneider, R. Ramos, J. Cramer, O. Gomonay, M. Filianina, T. Savchenko, D. Heinze, A. Kleibert, E. Saitoh, J. Sinova, and M. Kläui, Full angular dependence of the spin Hall and ordinary magnetoresistance in epitaxial antiferromagnetic NiO(001)/Pt thin films, Phys. Rev. B **98**, 024422 (2018).

[36] S. Seki, T. Ideue, M. Kubota, Y. Kozuka, R. Takagi, M. Nakamura, Y. Kaneko, M. Kawasaki, and Y. Tokura, Thermal Generation of Spin Current in an Antiferromagnet, Phys. Rev. Lett. **115**, 266601 (2015).

[37] W. Yuan, J. Li, and J. Shi, Spin current generation and detection in uniaxial antiferromagnetic insulators, Appl. Phys. Lett. **117**, 100501 (2020).